Biophysical Journal Volume 103 December 2012 2432–2445

Spatial and Temporal Sensing Limits of Microtubule Polarization in Neuronal Growth Cones by Intracellular Gradients and Forces

Saurabh Mahajan and Chaitanya A. Athale*
Division of Biology, Indian Institute of Science Education and Research-Pune, Pune, India

ABSTRACT Neuronal growth cones are the most sensitive among eukaryotic cells in responding to directional chemical cues. Although a dynamic microtubule cytoskeleton has been shown to be essential for growth-cone turning, the precise nature of coupling of the spatial cue with microtubule polarization is less understood. Here we present a computational model of microtubule polarization in a turning neuronal growth cone. We explore the limits of directional cues in modifying the spatial polarization of microtubules by testing the role of microtubule dynamics, gradients of regulators, and retrograde forces along filopodia. We analyze the steady state and transition behavior of microtubules on being presented with a directional stimulus. Our model makes novel, to our knowledge, predictions about the minimal angular spread of the chemical signal at the growth cone and the fastest polarization times. A regulatory reaction-diffusion network based on the cyclic phosphorylation-dephosphorylation of a regulator predicts that the receptor-signal magnitude can generate the maximal polarization of microtubules and not feedback loops or amplifications in the network. Using both the phenomenological and network models, we have demonstrated some of the physical limits within which the microtubule polarization system works in turning the neuron.

INTRODUCTION

A long-standing goal in developmental biology has been to understand the process of neuronal path-finding that results in the complex wiring seen in the nervous system. Studies have unraveled multiple cues that provide directional signals to the axon. Once the directional cue is detected by the growth cone (GC) at the end of an axon, the intracellular cytoskeleton undergoes polarized growth. The signaling networks that transduce an extracellular directional cue into cytoskeletal polarization during a neuronal GC guidance show striking similarities with those in highly migratory cell types such as slime molds *Dictyostelium*, neutrophils, and migratory fibroblasts (1). This diversity of cell types suggests an evolutionarily conserved set of mechanisms in cell guidance. Experimental work in nerve GCs has shown both actin and microtubule dynamics to be essential (2). Although many studies have investigated the role of actin in filopodial and lamellipodial dynamics in neuronal growth cones, the precise role of microtubules (MTs) is less well studied (reviewed in Gordon-Weeks (3)). MTs have been hypothesized to function like a cellular compass, which, by random fluctuations, searches directional space. In the presence of a cue, a reinforcement of the direction by transport of actin polymerization factors and membrane vesicles leads to turning of the GC (4). Thus, MT polarization appears to be an important early event in GC turning, but consists of a complex interplay of chemical and mechanical effects.

The chemical regulation of MTs in neuronal growth cones is through modulation of MT dynamic instability—the property of MTs to transition from a growing state to a shrinking state (catastrophe) and vice versa (rescue) (5,6). This dynamics has been shown experimentally to be essential for growth-cone turning (2,7–10) and is most sensitive to the frequency of catastrophes (11). Important regulators of length dynamics is a family of neuron-specific proteins of the stathmin (Op18) family—stathmin 2 (SCG10) and stathmin 3 (SCLIP) (12). The protein SCG10 destabilizes MTs by increasing catastrophe events; phosphorylation results in stabilized MTs, corresponding to decreased catastrophe events (13,14), in a manner similar to stathmin. SCG10 levels in primary cultured neurons appear to be critical for maintaining a balanced level of MT dynamics to enable neurite extension (15) and in vivo experiments indicate the *n*-methyl D-aspartic acid (NMDA) receptor (NMDAR) activation regulates SCG10 phosphorylation through ERK2 (16).

Mechanical force generated by the retrograde flow of actin flowing inwards from filopodial tips regulates the number and velocity of MT ingress into filopodia in neuronal growth cones (17). The coupling of the actomyosin-driven flows with the MT system is thought to occur through discrete sites of binding by factors with either the actin- and microtubule-binding activity (e.g., formins) or complexes of factors that have such activity (18). An additional force acts in the opposite direction of the retrograde flow driven by cytoplasmic dynein, which works to translocate microtubules toward the neuronal periphery as well as hold them in place in the filopodia (19).

Theoretical models and simulations have been used to model some subcellular aspects of neurons, providing insights into their dynamics. The cytoskeletal dynamics in growth-cone polarization was modeled in filopodial dynamics, which was itself modeled to be randomly searching space (20). A model of microtubule assembly and

Submitted July 21, 2012, and accepted for publication October 10, 2012.
*Correspondence: cathale@iiserpune.ac.in
Editor: Michael Edidin.

0006-3495/12/12/2432/14 $2.00
http://dx.doi.org/10.1016/j.bpj.2012.10.021

tubulin transport could reconcile the constant elongation rates of neurites with tubulin assembly processes (21). Complex two-dimensional models, which include the retrograde flow of actin, suggest a nonrandom mode of MT invasion of filopodia (22). A recent detailed model of retrograde actin flow and myosin contractility has revealed the balance of forces driving the flow in neurons (23). However, all these models ignore the chemical regulatory elements that play a crucial role in neuronal cytoskeletal dynamics. Independently, chemical spatial gradients have been modeled in MT spindle assembly (24) and cell polarization (25).

Previous modeling of reaction-diffusion gradients and their regulation of MT dynamics has been used to explain the nonrandom growth of MTs in mitosis (26,27). More recently, models of signaling proteins in neuritogenesis have demonstrated the role of feedbacks (28) and of cell shape in axon determination (29). However, a neuronal growth-cone model that includes both regulatory reaction-diffusion components and the explicit MT dynamics and mechanics has not yet been developed, to our knowledge. Given the accumulating evidence for the importance of microtubule regulation in growth-cone guidance, a spatial model including MT and actin interactions, combined with spatial dynamics of signaling proteins that modulate MT growth, will be useful from both experimental and theoretical perspectives.

Here we develop a model based on *Aplysia* growth-cone geometry and dynamics with experimentally measured parameters. Such a model provides a platform for testing experimental hypotheses that can lead to extremely involved experiments. We develop two kinds of models: a phenomenological MT stabilization model, and an explicit biochemically realistic reaction-diffusion model of MTs in turning GCs. Some of the typical scenarios of GC turning by a diffusible cue and perturbations of the actomyosin system show good agreement with existing experiments. Additionally, we predict the minimal spatial and temporal detection limit. The maximal MT polarization angle shows good agreement with the maximal GC turning angle seen in experiments. The detailed, biochemically realistic, regulatory reaction-diffusion network model is biologically based on the cyclic phosphorylation-dephosphorylation of a microtubule destabilizer of the stathmin family, found in neurons. It predicts the most effective point of regulation in such a network. We have used both the phenomenological and network models to understand the physical limits within which the MT polarization system works in neurons that have detected a polarizing cue.

THEORY

Growth cone and axon shaft geometry

The neuronal growth cone (GC) and terminal axon shaft were modeled as two-dimensional objects. The geometry was inferred image analysis of published images of *Aplysia* bag cell neuronal growth cones (30) using ImageJ (31) and a routine developed in-house using MATLAB R2008b (The MathWorks, Natick, MA). A circle of radius 25 μm is used to represent the growth cone based on dimensions of *Aplysia* growth cones. The GC is divided into concentric circles with the outer peripheral P-domain (radius 10 μm), the intermediate region transition T-zone (radius 5 μm), and the innermost central C-domain (radius 10 μm). The confining boundary is modeled as set of connected points with stiffness set to 100 pN μm, making it effectively rigid. A rectangular region, representing the axon shaft, emerges from the lower end of the circular GC. Based on reports of microtubule bundling by actomyosin forces in the growth-cone neck (32), a continuous spatial force field (Fig. 1 *A*) was implemented. For every fiber model-point lying in this field, the value of the force at the corresponding position in the field is added to the net force on the point.

Microtubule orientation and dynamics

Microtubules were implemented as elastic, nonextensible, polar fibers represented by a set of discrete model-points. The flexural rigidity (or bending stiffness) of microtubule fibers was set at 20 pN-μm^2 (33,34), which corresponds to a persistence length of 4.67 mm. Bending of these fibers at a shorter lengthscale is possible, though, based on the rigidity and force applied (35,36). To maintain the simplicity of the model, we do not model microtubule breakage. The fibers were modeled to be dynamic based on the four-parameter model (11): growth (v_g), shrinkage velocities (v_s), frequency of rescue (f_{res}), and catastrophe (f_{cat}). The parameters were spatially inhomogeneous with dynamic instability parameter values different for each of the domains as described in Table 1. These parameters affect only the plus-tip that enters it. An additional cortical catastrophe was modeled within 1 μm of the membrane periphery of the growth cone.

A fixed number of free microtubules ($N_{MTs} = 30$) are initialized with lengths randomly assigned between 16 and 24 μm by a uniform random-number generator with a total angle of 106° symmetrically about the vertical axis in an arc centered below the center of the circular GC (Fig. 1 *A*). This geometry is based on *Aplysia* growth-cone micrographs. The modeled MTs are dynamic at both ends. The parameters of dynamic instability, i.e., the frequencies of catastrophe and rescue, and the velocities of growth and shrinkage, are distributed inhomogeneously as functions of radial position in the GC (Fig. 1 *A*). Inside the axon-shaft, minus-ends of the modeled MTs undergo rapid catastrophe. The field of dynamic instability is set to a high f_{cat} value (destabilizing) in the P-domain, while the T-zone and C-domain have a stabilizing effect (Fig. 1 *A*).

The minus-ends of the MTs were initialized 20 μm below the point of contact of the axon shaft with the growth cone in

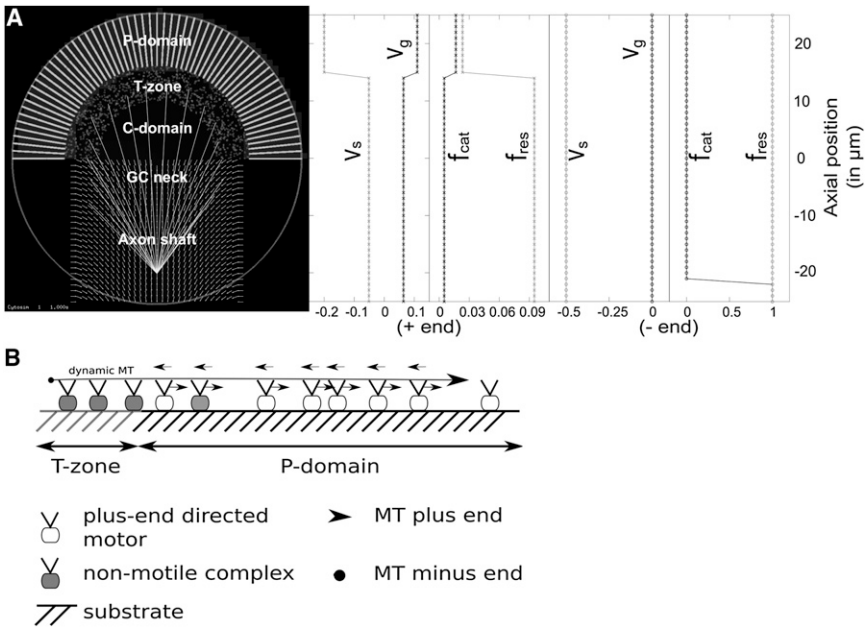

FIGURE 1 Geometry of growth-cone MT-motor system. (*A*) Semicircular geometry represents the growth cone, which is divided into three concentric regions: P-domain, T-zone, and C-domain. The C-domain is connected to an axon shaft. MT stabilization zone in the P-domain promotes MT polymerization. Immobilized plus-end directed motors are arranged in 61 symmetric radial arrays spaced at intervals of 3° in the P-domain. Nonmotile motors similarly immobilized are localized in the T-zone. (*Light* and *dark regions*, a subset of simulation space) Reaction-diffusion system is bounded. An effective force field in the GC-neck and axon shaft represents a compressive force (*white arrows*). Spatially distributed dynamic instability parameters v_g, v_s, f_{cat}, and f_{res} for the plus- and minus-ends are plotted along the GC-axon axis. (*B*, *Schematic*) Geometry of the modeled MT-motor interactions in the T-zone with nonmotile complexes and in the P-domain with plus-end directed motors.

the axon shaft. The minus-ends are dynamic, and undergo catastrophes if they move beyond a 20-μm radial distance from the center due to a spatial change in the catastrophe frequency to $f_{cat} = 1\ s^{-1}$. This occurs while the other parameters remain constant ($v_s = 0.5\ \mu$m/s, $f_{res} = 1\ s^{-1}$, and $v_g = 0\ \mu$m/s).

Force due to actin retrograde flow in the P-domain

The actomyosin retrograde flow is modeled by discrete immobilized motors arranged radially along filopodial bundles that push MTs inwards toward the C-domain (Fig. 1 *B*), based on reports in the literature of coupling-molecules that can bind to MTs and actin simultaneously. In filopodia, the actin itself is flowing inwards in a myosin-dependent retrograde flow, hence generating many point forces that pull MTs into the center of the GC. Recent reports on the role of kinesins in MT growth and polarization in the P-domain suggest that both the actomyosin system and a kinesin-based retrograde force are involved in moving MTs inwards from the periphery (37). Assuming both these systems act along the same direction, the force vectors due to actomyosin and kinesin activity can be added together, resulting in a high-stall force value (f_{stall}) (Table 2). Control calculations showed this force is sufficient to move MTs of a fixed length inwards with a retrograde flow speed that agrees with experimental measurements (17).

Motors-MT interactions are modeled as a Hookean spring in which a force exerted by a motor on a point of the fiber is given by $f_{ex} = k * \delta r$, where k is the stiffness and δr is the distance separating the motor and the point on the fiber. Motors were characterized by their positions, attachment/detachment rates (r_{attach}/r_{detach}), speed of movement (v_{mot}), direction of movement, stall force (f_{stall}), and stiffness (k) of the induced links. Detachment rate depends on the force generated as modeled previously (38) by

$$r_{detach} = r'_{detach} * exp\left(2 * \frac{|f_{ex}|}{f_{stall}}\right),$$

TABLE 1 Parameters of dynamic instability

Location of MT plus-end	P-domain	T- and C-domain	Reference
$v_g(\mu m\ s^{-1})$	11.5×10^{-2}	6.4×10^{-2}	Schaefer et al. (17)
$v_s(\mu m\ s^{-1})$	20×10^{-2}	5.1×10^{-2}	Schaefer et al. (17)
$f_{cat}(s^{-1})$	1.7×10^{-2}	0.5×10^{-2}	Schaefer et al. (17)
$f_{res}(s^{-1})$	2.3×10^{-2}	9.5×10^{-2}	Schaefer et al. (17)

Dynamic instability parameter values were chosen for the P- and C-domains and T-zone based on published values from *Aplysia* neuronal GCs.

TABLE 2 Motor parameters

Parameter	P-domain	T-zone	Reference
Number of motors	30,000	1000	Optimized
Speed v_{mot} (μm/min)	4.2	0	Schaefer et al. (17)
Binding rate r_{attach} (s^{-1})	5	5	Optimized
Unbinding rate r_{detach} (s^{-1})	1	1	Optimized
Maximum stalling force f_{stall} (pN) (kinesin and actin-retrograde flow)	15	15	Nadar (37), Medeiros et al. (67), Coppin et al. (68)
Attach distance (μm)	0.1	0.1	Optimized
Motor stiffness k(pN/μm)	100	100	Coppin et al. (68), Howard (69)

Parameters of surface-immobilized motors were chosen for the P-domain and T-zone to fit the retrograde flow rates and effective translocation speeds of MTs reported (17).

based on Kramers theory (39). The filopodial arrays ($n = 61$) are arranged between 0 and 180° with respect to the positive X axis through the semicircle of the GC with 30,000 motor complexes randomly distributed (uniformly) among the filopodial bundles (~500 motors per bundle). The speed of these motor complexes was set to 0.07 μm/s while attachment-detachment rates were optimized (see Table 2) to provide net translocations velocities in agreement with measurements in *Aplysia* growth cones (17).

In the T-zone, an analog of immobilized nonmotile dynein motors is modeled with $r_{attach} = 5$, $r_{detach} = 0.1$, and $v_{mot} = 0$. These motors hold MTs but do not move the microtubules when bound (Fig. 1 *B*).

Reaction-diffusion network model of receptor-driven intracellular polarization

This is a simple reaction-diffusion network consisting of three species: two cytosolic diffusive species which are assumed to be stathmin S and its phosphorylated form S^*, and a membrane immobilized receptor species (R). An optional positive-feedback interaction (by growing microtubule plus-tips (N_{tips}) and a weight of the feedback (w_1)) was implemented. This feedback increases the $S \rightarrow S^*$ conversion in presence of growing plus-tips. The value S is hypothesized to be phosphorylated to S^*, similar to stathmin phosphorylation, near the membrane by the receptor R, mimicking the NMDA-Erk2 pathway. The backward reaction converts S^* to S homogeneously in the cytosol governed by a first-order rate constant k_2. In the positive-feedback model, growing MT plus-tips can also enhance this forward reaction. The forward reaction is modeled using Michaelis-Menten kinetics as

$$\frac{d[S]}{dt} = -\frac{k_1[R][S]^{n_1}}{K_{M1} + [S]^{n_1}} - N_{tips}\cdot\frac{k_{fb}\cdot w_1\cdot[S]^{n_2}}{K_{M2} + [S]^{n_2}} + k_2[S^*] + D_S\cdot\nabla^2[S]. \quad (1)$$

The backward reaction is modeled using first-order kinetics as

$$\frac{d[S^*]}{dt} = \frac{k_1[R][S]^{n_1}}{K_{M1} + [S]^{n_1}} + N_{tips}\cdot\frac{k_{fb}\cdot w_1\cdot[S]^{n_2}}{K_{M2} + [S]^{n_2}} - k_2[S^*] + D_{S^*}\cdot\nabla^2[S^*]. \quad (2)$$

The terms n_1 and n_2 correspond to cooperative Hill-coefficients for the forward reaction and the MT-dependent feedback terms, respectively. These terms represent cooperativity in phosphorylation (n_1) or the positive feedback (n_2), due to either the extracellular regulated kinase (ERK) pathway (40) or multiple sites of phosphorylation in stathmin (41). Unless explicitly stated, the Hill-coefficient parameters were set to $n_1 = n_2 = 1$. Diffusion coefficients of the two diffusing cytosolic species S and S^* are given by D_S and D_S^* while the concentration gradient is indicated by the two-dimensional Laplacian ∇^2.

The role of S in modulating MT dynamics was implemented by increasing the local catastrophe frequency f'_{cat}, dependent on $[S]$ using a phenomenological expression described previously based on in vitro data (42):

$$f'_{cat} = f_{cat}\cdot exp(w_2\cdot([S] - [S_{tot}])). \quad (3)$$

Here f_{cat} is the default value (Table 1), when $[S] = [S_{tot}]$, $[S]_{tot}$ is the sum concentration of modified and unmodified stathmin, and $w_2 = 0.3144$, a scaling factor obtained by fitting to experimental data (42). The parameters used for the reaction-diffusion network are taken from the literature and described in Table S1 in the Supporting Material.

METHODS

Simulation of the microtubule model

Our model is implemented and simulations conducted using Cytosim—a cytoskeleton simulation engine implemented in C++ (43). All simulations were run for 1200 s (or more). Typical simulations include 30 dynamic MTs, 30,000 surface-immobilized motors in P-domain, and 1000 grafted motors in T-zone. The reaction diffusion system was simulated with spatial resolution of 1 μm. Positions of all objects and occurrence of events like movement, binding/unbinding, change in length of MTs (due to growth/shrinkage), and change in MT end-state (due to catastrophe/rescue) is calculated for all objects at each time step from the corresponding rate parameters. Simulations were run on a 12-core T5500 workstation (Dell, Round Rock, TX) with 2.40 GHz processors using a publicly available parallel processing code (Distributed Parallel Processing Shell Script, Ver. 2.85; http://www.gnu.org/licenses/gpl.html). Each typical run takes ~1500 s to complete.

For each iteration, total MT numbers, mean direction of MT distribution, and circular spread of MTs were calculated in the P-domain and angular trends were analyzed in 12 angular sectors of 15° each (Fig. 2 *C*). The mean-angle of MT distribution in a GC at a time point (t) was calculated as

$$\theta_{av}(t) = \frac{\Sigma N^i_{tips}\cdot\theta_i}{\Sigma N^i_{tips}}, \quad (4)$$

where θ_i is the midangle and the value N^i_{tips} signifies the number of plus-tips in the i^{th} sector. The corresponding circular standard deviation ($\sigma_c(t)$) is given by

$$\sigma_c(t) = \sqrt{\frac{\Sigma N^i_{tips}\cdot(\theta_i - \theta(t))^2}{\Sigma N^i_{tips}}}. \quad (5)$$

Time averages of mean-angle ($\langle\theta_{av}\rangle$) and circular standard deviation ($\langle\sigma_c\rangle$) were used as measures to compare with experiments. In experiments where a directional bias was introduced, differences between mean-angles averaged at steady state before and after the bias ($\Delta\langle\theta_{av}\rangle$) were evaluated as a measure of MT polarization.

Simulation of the reaction-diffusion model

The two-dimensional system of partial differential equations was solved on a finite lattice grid by using an explicit forward-difference scheme

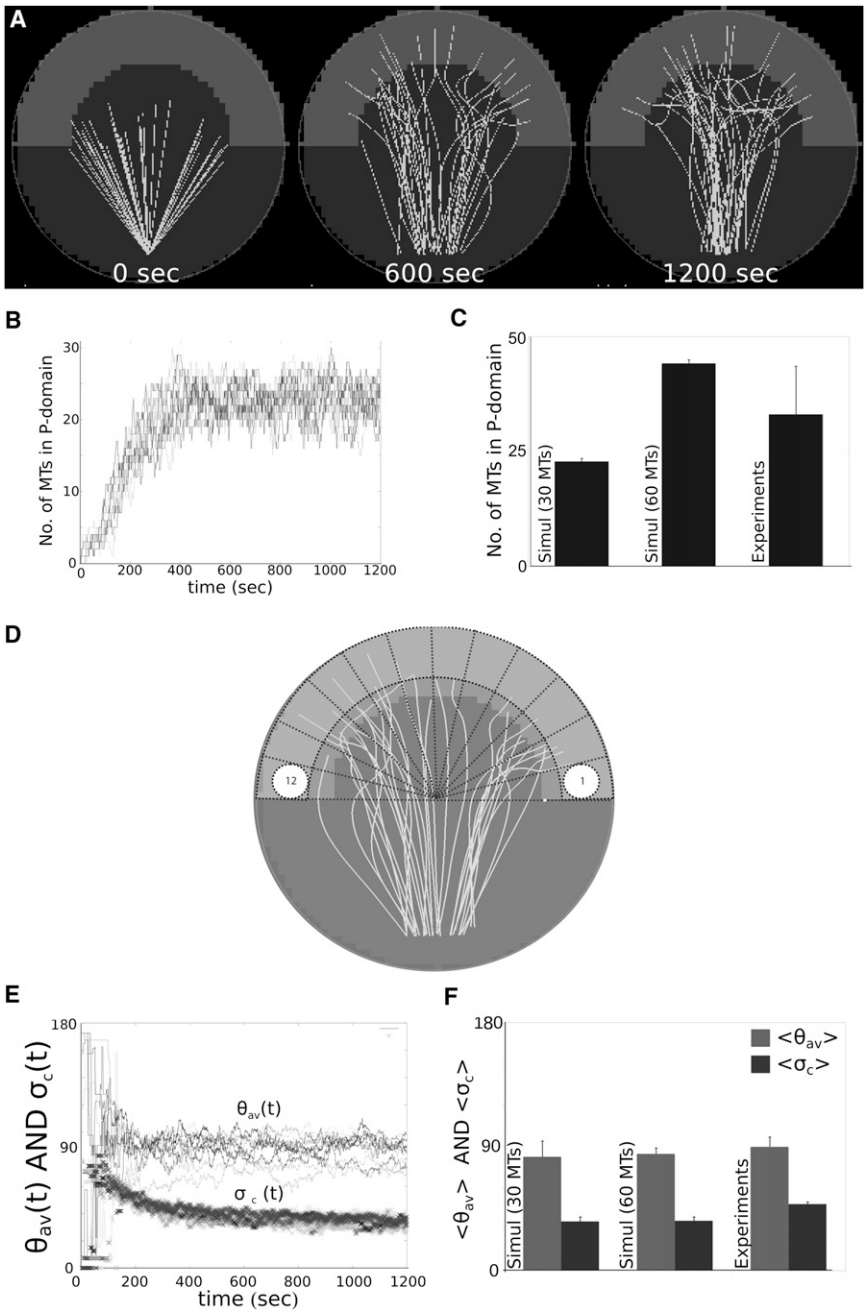

FIGURE 2 MT dynamics in an unbiased growth cone. (*A*) Time-series of MTs entering the P-domain (the region with higher catastrophe frequencies) in simulation snapshots at 0, 600, and 12,000 s is represented in two-dimensional plots and (*B*) as a time course of MTs entering the P-domain and achieving a fluctuating steady state. (*C*) At steady state, the number of MTs in the P-domain in simulations with 30 or 60 initialized MTs was compared to images from experiments ($n = 2$) (17,32). (*D*) Geometry of the growth-cone angular sectors is schematically represented. (*E*) This is used to calculate the time-dependent mean-angle of MTs ($\theta_{av}(t)$) and its standard deviation (SD) ($\sigma_c(t)$). (*F*) Simulated mean-angle and spread at steady state ($t > 400$ s) was compared to experimental distributions ($n = 2$) (17).

(44). The spatial interval $\Delta x = 1$ μm and time interval $\Delta t = 0.01$ s were optimized by comparing simulation results with analytical solutions of known initial condition cases (see Fig. S4 in the Supporting Material) (45). Zero-flux boundary conditions were used at the growth cone and axon-shaft boundaries (Fig. 1 *A*). All preliminary calculations were performed in Octave (46) and then implemented in C++.

Analysis of experimental MT distributions

Images of fluorescently labeled microtubules in *Aplysia* growth cones were analyzed in-house using a MATLAB script (The MathWorks) and the software ImageJ (National Institutes of Health, Bethesda, MD) combined with manual counting of plus-tips.

RESULTS

Microtubule angular distribution is uniform and fluctuating

A two-dimensional model of the *Aplysia* growth cone with dynamic MTs has been developed to understand the quantitative details of spatial remodeling of MTs in the earliest events relating to neuronal growth-cone turning. The model integrates MT regulatory and mechanical components, as described in Methods. The simulation geometry with spatial dynamic instability and filopodial geometry is shown in Fig. 1 *A*. A radial inward-directed retrograde flow and

dynein-based stationary coupling of MTs is modeled using a motor model geometry schematically illustrated in Fig. 1 *B*. A simulation run of such a model shows MTs entering the P-domain in ≈10 min to attain a uniform but fluctuating distribution (Fig. 2 *A*, and see Movie S1 in the Supporting Material). We also observe some MT buckling mostly in the T-zone. This geometry and dynamics are qualitatively similar to in vitro data of *Aplysia* growth cones.

The quantitative dynamics of MTs entering the P-domain also show rapid steady state where, on average, two-thirds of the MTs remain in the P-domain (Fig. 2 *B*). The fluctuations suggest that MTs can constantly search the P-domain for directional cues, primed for turning. The number of MTs in P-domain for two different values of initialized MT numbers (30 and 60) show between 25 and 50 MTs on average (Fig. 2 *C*). This is in agreement with previous experimental observations (17,32). The spatial patterns of these MTs were analyzed by sampling the number of plus-tips in discrete angular periods for each time point (Fig. 2 *D*). The weighted mean angle for the MTs in the P-domain of a GC was calculated based on Eq. 4 and plotted against time (Fig. 2 *E*). After initial fluctuations, θ_{av} reaches a steady-state value of ≈90° in ~300 s of simulations, while the corresponding circular standard deviation ($\sigma_c \approx \pi/6$) calculated from Eq. 5 achieves a steady-state value of ~45°. The time-averaged mean MT angle ($\langle\theta_{av}\rangle$) is as expected ~90° ($\langle\sigma_c\rangle \sim 30°$), independent of the number of MTs simulated (Fig. 2 *F*). Both the mean-angle and the circular standard deviation are in good agreement with experimental measures (17,32). Simulations of MT density dynamics in four equal sectors of the GC for initial MTs $N = 30$ (Fig. 3 *A*), $N = 60$ (Fig. 3 *B*), and $N = 90$ (Fig. 3 *C*) are all of the same order of magnitude as experiments with *Aplysia* growth cones (47).

To test whether the standard model of motor detachment based on Kramers theory affects our results, a simple model with constant rates of motor detachment in the P-domain was tested. The values r_{detach} 1 s^{-1} or r_{detach} 5 s^{-1} are the two extreme values from a two-state, load-dependent detachment model that was shown to better-fit experimental data for kinesin (48). The mean MT number in the P-domain and the mean-angle remain unchanged (see Fig. S1), suggesting little effect of changing detachment rates.

Thus, our model simulations show, qualitatively and quantitatively, expected behavior in agreement with the available spatial and dynamic data. In the following sections, we perturb this model system and compare it with experiments.

A decreased retrograde flow rate results in increased MT flux in the P-domain

The role of the actomyosin retrograde flow was explored in our modeled growth cones by analyzing its effect on the flux of MTs entering the P-domain. A reduction of 50% in the retrograde flow rate (from 4.2 μm/min to 2.1 μm/min) results in a twofold increase in MT-tip flux only in the peripheral 25% of the modeled growth cone (Fig. 3 *D*). Such a dramatic effect is not observed if larger proportions (50% and 75%) of the P-domain were sampled. This suggests the fluctuations in the most distal region of the growth cone are the ones most sensitive to such treatment. On the other hand, a twofold increase in retrograde flow rate results in an ≈85% decrease in flux of MT tips in the distal 25% of the P-domain.

This effect is also seen in experimental analyses of MT dynamics, which report MT fluxes only in the distal 25% of the GC. The effect of changing retrograde flow rates on absolute number of MTs in the P-domain shows small but statistically significant differences (Fig. 3 *E*). The relative proportion of simulated MTs ($N = 30$) compared to those entering the P-domain also progressively diminishes if we observe the most peripheral 25% of the growth cone. Experimental measurements of the flux of MT plus-tips within neuronal growth cones perturbed by blebbistatin—a myosin II ATPase inhibitor—indeed showed that a 50% decrease in retrograde flow rates results in a twofold increase in the flux of MTs entering the P-domain in the peripheral 25% of the P-domain (30). This correspondence with experimental data shows our model of retrograde flow can be used for further studies on MT dynamics modulation.

A spatial catastrophe frequency change is most effective in changing the polarization angle of MTs

Recent evidence has been accumulating for the role of MT polymerization modulation in GC-turning. We have systematically tested the role of MT dynamics in MT polarization, an early event in GC-turning. Values of dynamic instability were modified in only one-half of the P-domain of the simulated growth cone. The result of this spatial bias was evaluated by plotting a time course of the $\theta_{av}(t)$. Although fluctuations in the mean MT-angle remain large, a small change in mean-angle is observed from the unbiased base (Fig. 4 *A*). Both the actual simulation (see Movie S2) and a time-averaged angular distribution of the MTs, before and after bias in the control case compared to the biased case, represent this change more graphically (Fig. 4 *B*). To test the parameter to which the system was most sensitive, the bias was systematically introduced in each of the parameters of dynamic instability (f_{cat} and f_{res}). The change in mean-angle ($\Delta\langle\theta_{av}\rangle$) of MTs in the outer-half of the P-domain was evaluated and compared to the control (*cat*/*res*) (Fig. 4 *C*). Increasing catastrophe frequency turns the mean-angle of MT distribution away from the direction of bias, while the increase in rescue frequency turns the MT distribution toward the bias. The 10-fold increase in f_{res}, 10-fold decrease in f_{cat}, and 10-fold increase in f_{cat} show the significant changes in mean-angles compared to the unbiased case (two-way Student's *t*-test $p < 0.05$). A

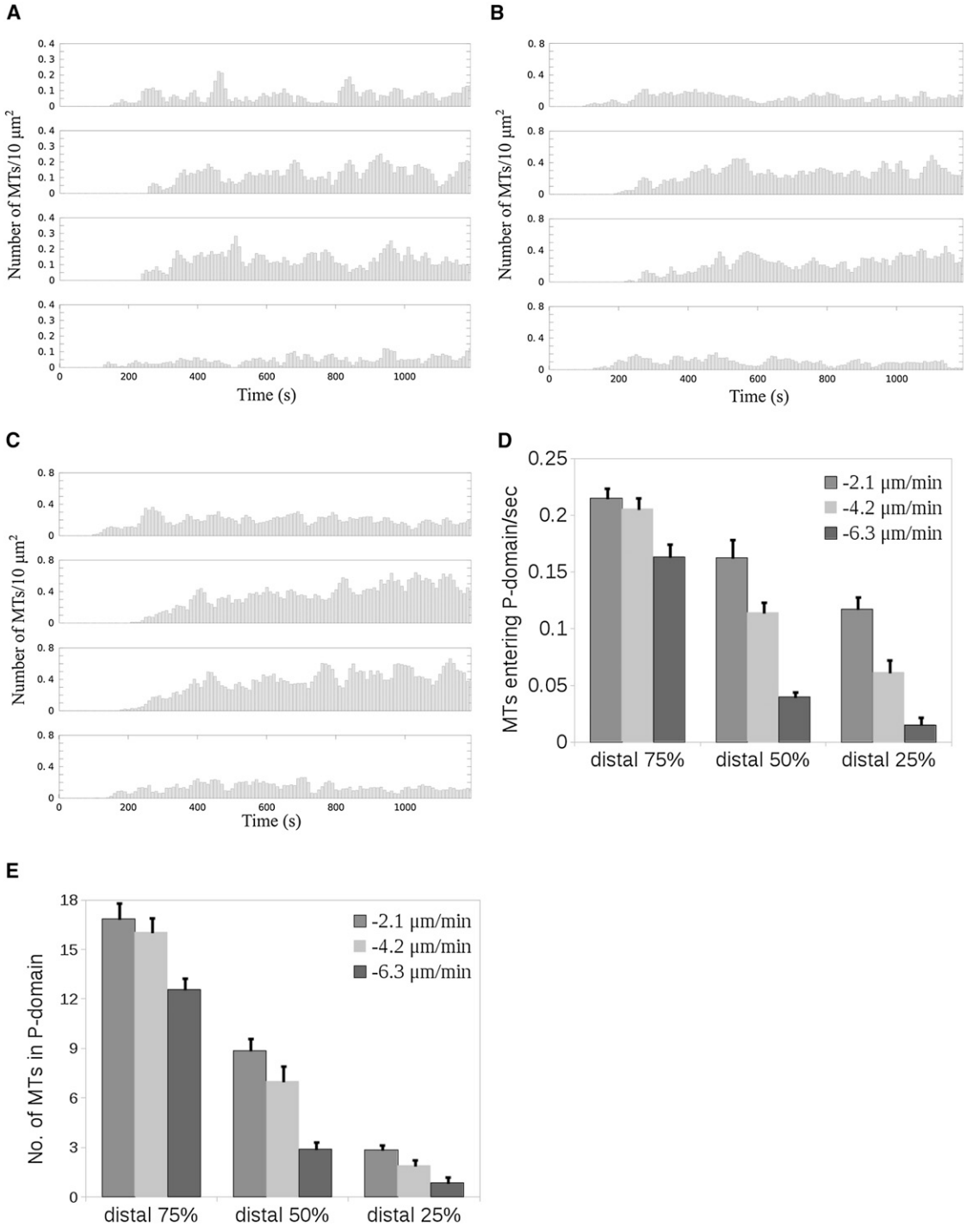

FIGURE 3 Effects of perturbing the number of MTs and retrograde translocation rates MT densities in the peripheral 25% of the growth cone are plotted against time for initial nucleated MTs numbering. (*A*) 30, (*B*) 60, and (*C*) 90. (*D*) Number of MTs entering the P-domain per second show a 50% change when standard retrograde translocation speeds (4.2 μm/min) are changed by 50%. This effect is visible in the most-distal quarter of the P-domain and not as pronounced when larger elements (50–75%) of the P-domain are sampled. (*E*) Absolute number of MTs in the P-domain is less dramatically affected by changes in retrograde translocation speeds. Error bars are SD (iterations $n = 10$). (*Stars*) Statistically significant differences from the control case.

10-fold decrease in f_{res} does not result in a significant change in mean-angle of MTs.

To further examine the minimal range within which the rescue and catastrophe frequencies change the mean-angles of MT, stepwise increases in f_{res} and f_{cat} were made. Statistically significant changes in $\Delta\langle\theta_{av}\rangle$ were observed even with two- and fourfold changes in f_{cat} and f_{res} values (Fig. 4 *D*). These results suggest even a small change in

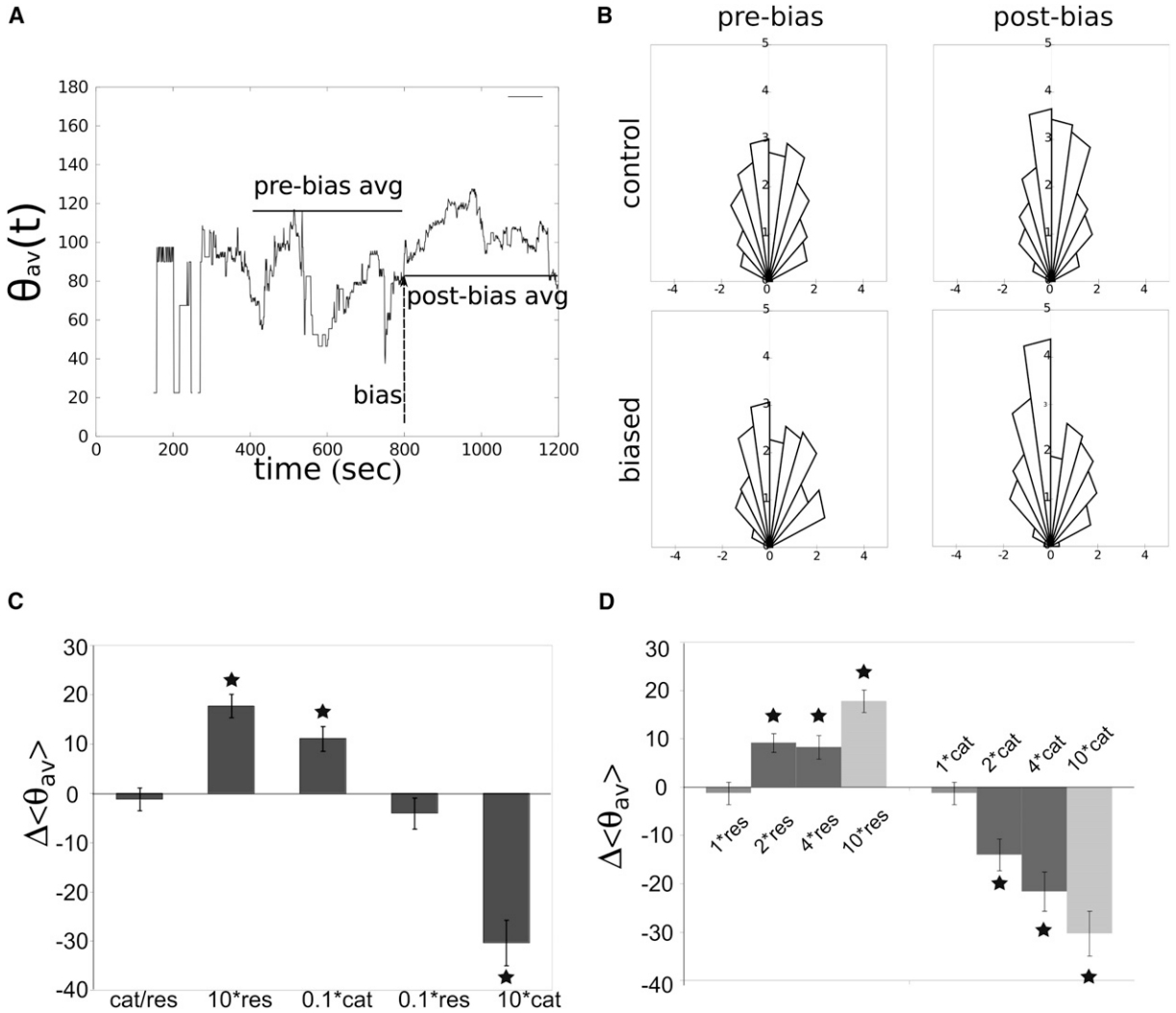

FIGURE 4 MT polarization in a biased growth cone. (*A*) Time-dependent mean-angle ($\theta_{av}(t)$) of MTs shows a change in mean direction when a directional bias is introduced in the left-half of the GC at 800s by decreasing f_{cat} 10-fold. (*B*) Angular frequency distribution of the mean number of MTs at steady state shows a clear polarization in the biased case. Sectors are 15° apart while the radial distance from the origin indicates the number of MTs (iterations $n = 10$). (*C*) Mean change in angle of MTs after the bias ($\Delta\langle\theta_{av}\rangle$) is the greatest for a 10-fold increase in the f_{cat} values in one-half of the GC, but the change is also statistically significant (*star*) for an increase in f_{res} and decrease in f_{cat}. (*D*) Fold changes in f_{cat} and f_{res} biases (iterations $n = 10$) show statistically significant changes (*star*) for twofold-or-greater changes in both parameters. Error bars indicate standard errors ($n = 10$).

dynamic instability can bias a the MTs in the given geometry; however, changes in the f_{cat} values produce the most dramatic effect on $\Delta\langle\theta_{av}\rangle$. These results are consistent with previous nonspatial models of MT dynamics that demonstrated theoretically as well as experimentally (in mitosis) that the mean MT length is most sensitive to changes in f_{cat} (11). This also sets the stage for testing the spatial limits of MT polarization in our model growth cones.

Spatial and temporal limits to MT polarization sensitivity

To test the sensitivity of the MT polarization system in the modeled growth, we modeled different extents of the polarizing cue and evaluated the output. The sensitivity was estimated in two ways:

1. the change in mean-angle ($\Delta\langle\theta_{av}\rangle$) as a function of the angular extent of the bias, and
2. the time taken for the adaptation, i.e., the new steady state.

In simulation, f_{cat} values were decreased or f_{res} values were increased 10-fold in sectors of the P-domain. These sectors were all centered at ~120° and the angular extent was varied between 0 and 60°. The change in mean-angle $\Delta\langle\theta_{av}\rangle$ was reduced from $\approx 15°$ to $\approx 5°$, in response to changes in the catastrophe and rescue frequencies. The change in mean-angle with decreasing spread of f_{res} showed a seemingly steady polarization angle of $>10°$ for bias extents as small

as 30°. A rescue frequency bias <30° also resulted in a small but statistically significant change (Student's *t*-test) in the mean-angle (Fig. 5 *A*).

Reducing the spatial extent of f_{cat} resulted in a steady reduction in $\Delta\langle\theta_{av}\rangle$ with ever-decreasing spatial extent (Fig. 5 *B*). This result appears to contradict the observed maximal sensitivity of MT length to the catastrophe frequency. It is likely to be a result of the increased catastrophe frequencies at the GC periphery, which are better compensated by a higher rescue frequency. This prediction can also be experimentally tested, and would suggest alternative sensitivity of the MT system in realistic cell geometries as compared to in vitro or mitotic measurements. Additionally, it suggests that a measurable MT polarization cannot occur if the bias is smaller than 20° in angular extent for catastrophe frequencies, and 10° for rescue frequencies.

To test the temporal sensitivity of the polarization of MTs, one-half of a growth cone was biased by changing either f_{cat} or f_{res} abruptly. The time taken for adaptation was estimated by fitting the dynamics of the mean-angle of MTs in the growth cone ($\theta_{av}(t)$) to a simple saturation kinetic expression (Fig. 5 *C*),

$$\theta_{av}(t) = \theta_{av}(0) + \Delta\theta_{av}(t)\cdot\frac{t^n}{t^n + K_t^n}, \qquad (6)$$

where $\theta_{av}(t)$ is the mean direction at time-step t, $\theta_{av}(0)$ the mean direction before the bias is introduced, $\Delta\langle\theta_{av}\rangle$ is the net change in direction after the bias, n is the Hill coefficient, and K_t is the half-time within which polarization is half-complete. The change in K_t from the time of imposition of the bias is ΔK_t. A smaller value of ΔK_t indicates a faster response to the stimulus. Ten-fold increases and decreases (independently) in catastrophe and rescue frequencies produced ΔK_t values ranging from 30 to 45 s. A 10-fold decrease in rescue frequency could not be fitted by the routine. This appears to indicate a characteristic time for half-GC-bias experiments for MT polarization to be in the range of ≈30 s. This could be experimentally tested in a carefully designed experiment. At the same time, the phenomenological gradient of stabilization of MT growth in space must have an underlying mechanistic basis. Hence, we developed a spatially explicit reaction-diffusion model of a potential MT regulatory protein in the framework of the previously developed spatial MT dynamics in the neuronal growth cone.

A cyclical phosphorylation-dephosphorylation reaction-diffusion network leads to MT polarization

To test the role of a biologically realistic factor that can change microtubule dynamics, a reaction-diffusion spatial model of an MT regulator was developed, based on the role of the protein SCG10, the stathmin (Op18) homolog. We have simplified the network of ERK-dependent phosphorylation of stathmin to consider its core element, namely MT spatial regulation. In our model of stathmin (*S*), phosphorylation (*S**) occurs at the membrane due to a receptor (*R*) whereas dephosphorylation can occur throughout the GC, resulting in a gradient of f_{cat} (see Fig. S5). An additional feedback term (w_1) regulates further amplification of the phosphorylation reaction. Both *S* and *S** are modeled to be diffusible through the GC geometry, while *R* is

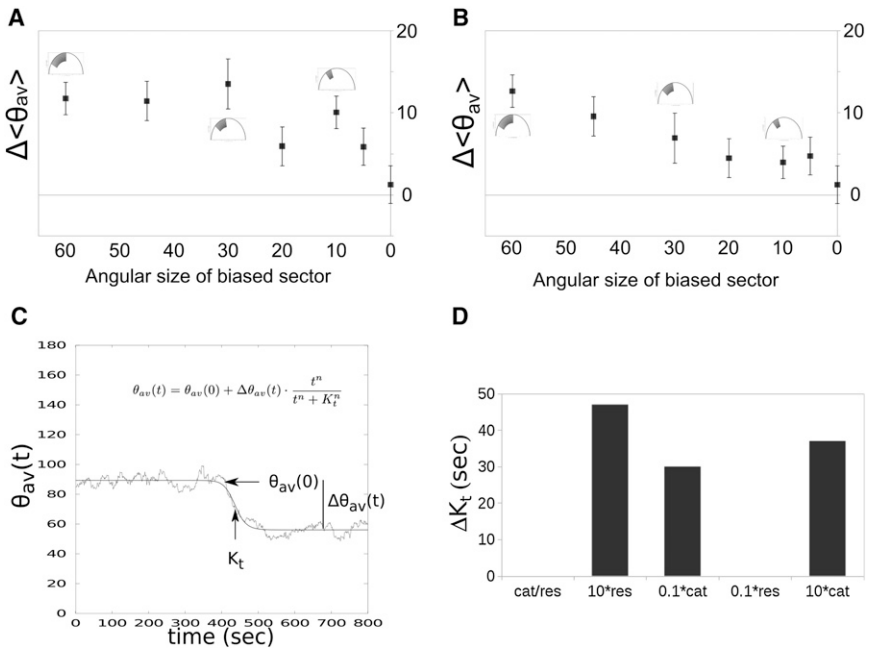

FIGURE 5 Spatial and temporal sensitivity. Decreasing angular sectors of the GC were biased by changing values 10-fold of (*A*) f_{res} (increased) and (*B*) f_{cat} (decreased). Sectors were centered around 120° (*striped*) with respect to the GC semicircle. Less broad biases in f_{cat} resulted in a steep reduction in MT polarization, while it remained fairly similar for f_{res} biases as narrow as 10°. Error bars indicate standard errors ($n = 10$). (*C*) Time taken for the half-maximal change in MT mean-angle after a bias is introduced (ΔK_t) was estimated by fitting the time-course of MT mean-angle ($\theta_{av}(t)$). (*D*) The most rapid change in MT mean-angle was produced by a 10-fold reduction in f_{cat}, whereas a similar reduction in f_{res} produced almost no change.

a parameter in the model, as seen in Eqs. 1 and 2. To test numerical stability of our integration scheme, the diffusion of a single species was compared to that in an analytical model (see Fig. S4). The modulation of MT dynamics occurs in our model by modifying the f_{cat} values based on Eq. 3. The resultant steady-state distribution in such a simple model of phosphorylation-dephosphorylation cycles demonstrates the differences in the spatial extent of S and S^*. This is in response to a stimulus in one-half of the GC as seen along the radial (see Fig. S5) and central (see Fig. S5) axes. The time course of gradient formation by depletion of S in one-half of the GC is visible in Movie S3.

To test which component of this reaction scheme might affect the polarization of MTs maximally, we compared the $\Delta\langle\theta_{av}\rangle$ for receptor signal strength and nature of the reaction kinetics. We tested the effect of changing the phosphorylation reaction of S to S^* transition from a simple first-order ($K_{M1}/[S_{tot}] = 2$), intermediate ($K_{M1}/[S_{tot}] = 1$), or zero-order saturated ($K_{M1}/[S_{tot}] = 0.1$) scenario. The effect of changing receptor concentrations $[R]$ (1, 10, 100, 200 μM) was simultaneously tested for each of the $K_{M1}/[S_{tot}]$ values. We find high-receptor-signal values lead to the most significant changes in $\Delta\langle\theta_{av}\rangle$ (Fig. 6 *A*). This is also borne out by the mean steady-state postbias angular distributions of MTs (Fig. 6 *B*). All reactions were carried out with the Hill-coefficient in the phosphorylation reaction set to $n_1 = 1$ (Eq. 1). For the situation of a high receptor stimulus ($[R] = 100$ μM), when n_1 was set to higher values (2,4,10) the polarization angle $\Delta\langle\theta_{av}\rangle$ did not change appreciably (see Fig. S3), indicating a negligible effect of the cooperative term.

The feedback from MTs to promote the phosphorylation reaction was simulated and compared to the model without feedback, in terms of the final readout for the f_{cat} distributions. The simple model demonstrates a slight but clear directional bias, whereas the feedback model in contrast shows local inhomogeneities in f_{cat}, corresponding to the presence of growing plus-tips (indicated by *arrows*) (Fig. 6 *C*). As a result, the mean postbias MT distribution is visibly polarized in the simple reaction case as compared to the strong feedback model (with both positive-feedback $w_1 = 200$ and Hill-coefficient $n_1 = 10$) (Fig. 6 *D*).

Taken together, these results suggest that a model of a stathminlike phosphorylation-dephosphorylation mechanism without feedbacks can indeed polarize microtubules in a neuronal growth-cone geometry. It remains to be seen whether such a gradient and downstream MT effect can be measured experimentally.

DISCUSSION

Cytoskeletal dynamics in GC turning has been increasingly seen as critical for understanding neuronal GC guidance (49) because multiple signaling pathways converge on the actin-microtubule system (50). As of this writing, very few of the details are known of this coupling between the signaling mechanisms with the cytoskeleton in neuronal growth cones. Previous studies have focused either only on the mechanics of cytoskeleton or the dynamics of the signaling system. Our study for the first time, to our knowledge, explicitly considers this coupling between microtubule mechanics and signaling gradients in a neuronal growth cone. We focus on the role of the spatial regulation of MTs in a turning GC. Another feature of our model is its comparison with previously published data of MT polarization in an *Aplysia* neuronal growth cone, thus making many aspects of our model biologically relevant and testable. All input parameters of microtubule dynamics and actin retrograde flows are taken from neuronal studies, except in the case of microtubule-motor mechanics and stathmin, where the parameters are derived from in vitro studies.

Our neuronal MT-polarization model is based upon the following assumptions:

Assumption 1: A static extracellular guidance cue.
Assumption 2: A single-step phosphorylation of the MT regulatory protein, ignoring intermediate steps.
Assumption 3: A phenomenological nonlinear mapping of stathmin concentration and microtubule dynamics.
Assumption 4: The two-dimensional geometry of the growth cone with the mechanics of retrograde pushing of MTs.

During the process of neuronal GC turning, the assumption of a static guidance cue holds true because the timescale of remodeling of the MTs is an order-of-magnitude slower than receptor polarization. For instance, MT polarization in *Aplysia* growth cones occurs within ~10 min (18,47), whereas receptor polarization of NMDAR takes only seconds (51,52). We use this difference in timescales to focus on the events slower than membrane-receptor polarization, i.e., downstream signaling and cytoskeletal regulation. The downstream signaling from these receptor signals, either through GTPases or through kinase-phosphatase systems, have a conserved modular structure that permits simplification of the cascade to a two-component cyclical reaction (53,54).

Using such a relatively simple single-step reaction cycle, we can also test multiple modes of amplification and feedback in a manner that is tractable. Such amplification steps are thought to be part of the mitogen-activated kinase (MAPK) extracellular-regulated kinase (ERK) pathway (40), upstream of the cyclical reaction. Although the Hill-cooperativity modeled in Eqs. 1 and 2 has not been measured in neuronal GCs, this model allows us to explore the multiple levels at which potential amplification of the reaction network can occur. The modeled two-dimensional geometry was assumed to be a reasonable approximation of the growth cone, based on micrographs of *Aplysia* bag-cell neuron growth cones that are typically 20–30 μm in diameter but only 2–3 μm in height in the P-domain (47).

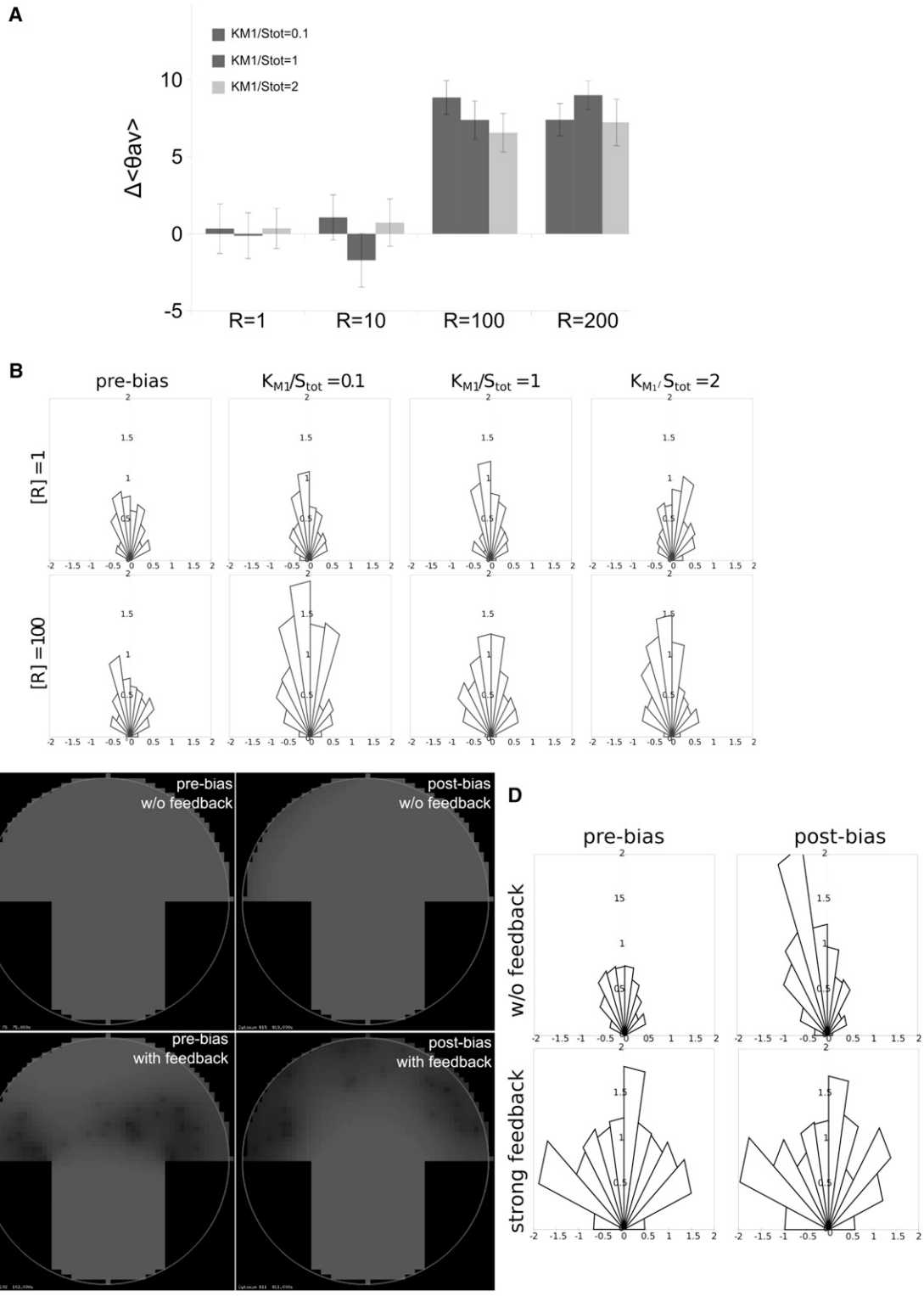

FIGURE 6 The amplification of the signaling system. (*A*) The polarization of MTs in response to zero-order ($K_{M1}/S_{tot} = 0.1$), intermediate ($K_{M1}/S_{tot} = 1$), and first-order ($K_{M1}/S_{tot} = 0.1$) reaction kinetics are compared to increasing values of the receptor signal ($n = 30$). (*B*) The schematic polar frequency distribution of the number of MTs shows the greatest polarization in the MTs in response to a first-order reaction kinetic with the highest receptor signal. (*C*) Spatial plots of S distribution in the GC are compared for two networks—the simple cyclic reaction without feedback ($R = 200$ μM, $K_{M1}/S_{tot} = 2$, $n_1 = 1$) and the growing MT-tip-driven positive feedback loop (with additional parameters $w_1 = 200$, $K_{M2}/S_{tot} = 0.1$, $n_2 = 10$). (*D*) Polar plots at steady state of number of MTs display a highly polarized distribution for the simple cyclic reaction without feedback, as compared to the strong feedback network.

Using this model, we compare our simulations to previously published experimental data. It is clearly seen that the mean-angle and spread of the modeled neuronal MTs are strikingly similar to the experimentally measured values from *Aplysia* growth cones in the absence of a directional cue (17,32). The simulated quadrantwise time-dynamic of MT densities in the peripheral 25% were plotted for GCs with the initial number of MTs as 30 (Fig. 3), 60 (Fig. 3), or 90 (Fig. 3). Agreement with experimental measures of MT density in the peripheral P-domain (47) and quadrantwise dynamics (10) is seen only for the MT numbers 60 and 90. However, the effective MT-flux rates in simulation (Fig. 3, and see Table S2) are similar compared to experimental values (30). Given the available data, the comparison of the change seen in MT flux in the peripheral 25% of the P-domain after a 50% reduction in retrograde flow rates is further evidence that the model of microtubule dynamics and geometry appears to be valid. The converse experiment of the increase in flux rates has been performed by small-interfering RNA inhibition of dynein in the GC, which opposes the retrograde flow. In experiments, this results in an approximately eightfold reduction in MTs in the peripheral P-domain (19)—a difference not seen in our model. However, the interpretation of the experiment, as well as differences among rat superior cervical ganglia neurons from *Aplysia* neuron sizes, could partly cause the difference. We also find that a spatial bias in the retrograde flow velocities can influence MT polarization in either a twofold increase or decrease in retrograde velocities (see Fig. S2). This makes our results comparable to selective inhibition of kinesin in only one-half of the GC, which resulted in growth cone turning (37).

A surprising property to emerge from our model simulations was the buckling of microtubules in the T-zone (Fig. 2). It results from the combination of the GC geometry, immobilized motor complexes of the T-zone, and actin retrograde flow in the P-domain. Such MT buckling has been previously observed in experimental measurements (17), and is thought to also result in breakage of MT fibers, which then either polymerize or are translocated toward the P-domain. In previous iterations of the simulation, it was found that the T-zone localization of immobile motor complexes was critical to maintain the orientation and spread of MTs as they enter the P-domain. Hence, our model would appear to suggest a functional role for such a set of complexes, which at first sight appear passive. Changing these complexes into minus-end-directed active motors increases the buckling of the MTs. A further quantification of this buckling both in experiment and theory might prove useful. These molecular motor assemblies might also play a role in the proposed polarity sorting of short microtubules in neurons, as previously proposed in qualitative models by Baas and Mozgova (55) and Baas and Yu (56). Our model could be used in future to test the specifics of such processes.

The sensitivity of the MT polarization system in response to changes in dynamic instability parameters was measured to give an idea of the ideal points of regulation. We found the system to be most sensitive to the frequency of catastrophe. However, statistically significant changes in mean MT angle were also observed as a result of fold-changes in both catastrophe and rescue frequencies. The change in mean MT angle is observed to be 20–30° for rescue and catastrophe frequencies. The experimental mean-turning-angle observed for *Xenopus* embryonic (57) and spinal neurons (58) as well as rat spinal neurons (59) were also in the range of ~20°. We consider this to be a strong, but qualitative, validation of our model of MT polarization.

Regarding the spatial sensitivity of the system, the model predicts that the attractive or repulsive cue needs to be spread across, minimally, a 30° angle of the growth cone. Most experiments of GC-turning involve a pipette assay where the chemical that provides the directional cue is applied extracellularly centered 45° to the GC and angular spread appears quite large (~90°)—difficult to control in such in vitro assays (60). However, bead-based assays (61) suggest an alternative method for estimating the role of spatial extent of the cue. The larger question of the in vivo scenario might also further complicate matters, with multiple cues simultaneously stimulating a single GC. We cannot resolve this in our simulation, although our model does predict a lower limit to the MT polarization system in the neuronal GCs, which can be experimentally tested. The guidance of neurons was shown to increase linearly with signal/noise ratio both in theory and experiment with rat dorsal-root ganglion explants (62). Our results are qualitatively comparable with previous data of increased MT polarization with increasing receptor concentration and broadening of the receptor signal, but a more detailed receptor-ligand dynamics model will be required for a direct comparison between the two models.

We further resolve our spatial MT polarization model of GCs by including a stathminlike regulator of MT dynamics and its cyclic phosphorylation-dephosphorylation, because stathmin has been shown to modulate MTs and affect neurite outgrowth in rat hippocampal neurons (15). The mapping from phospho-stathmin concentration to MT dynamics parameters, however, has been measured only in *Xenopus* oocytes (42) and we use the empirical fit to this data as a start point. This biologically realistic scenario is used to test the effect of different network topologies such as a feedback from MT tips to the reaction network and saturated reaction kinetics. We find these amplifications do not improve the angle of turning, as compared to the simple cyclic phosphorylation-dephosphorylation reaction system. The feedback from intact MTs appears in our system to amplify noise and cause spurious polarization even in the absence of a cue. On the other hand, we do find that receptor activation strength proves to be a much better means of strengthening the polarization of the MT system. This result

reveals an important design principle of such a system—namely, amplification steps appear more effective at the receptor-signaling level. This is consistent with recent findings in a simple model of MT-feedback-based GABA receptor polarization that amplifies receptor-based signaling (63). Our study goes beyond this to analyze the explicit regulation of MT dynamics by both chemical and physical mechanisms.

CONCLUSION

The model presented here predicts various mechanical and chemical properties of MT cytoskeleton regulation in neuronal GC turning. Validation with existing data demonstrates the utility of this model and points the way for additional experimental testing. The predicted physical limits to MT polarization in GCs are important, because it reveals potential design principles of neuronal GC turning. Additionally, recent developments in microfluidics and micropatterning techniques (64,65) suggest means of experimental testing of these predictions. The recent in vivo evidence from neuronal regeneration by MT stabilization (66) shows the growing need to understand the role of microtubule polarization at a system level in neurons. We believe this study is a step in this direction.

SUPPORTING MATERIAL

Two tables, four figures, and three movies are available at http://www.biophysj.org/biophysj/supplemental/S0006-3495(12)01126-5.

We thank Francois Nedelec for discussions regarding cytoskeletal simulations.

The work was supported by core funding from the Indian Institute of Science Education and Research-Pune, Pune, India.

REFERENCES

1. Parent, C. A., and P. N. Devreotes. 1999. A cell's sense of direction. *Science.* 284:765–770.
2. Mitchison, T., and M. Kirschner. 1988. Cytoskeletal dynamics and nerve growth. *Neuron.* 1:761–772.
3. Gordon-Weeks, P. R. 2004. Microtubules and growth cone function. *J. Neurobiol.* 58:70–83.
4. Andersen, S. S. 2005. The search and prime hypothesis for growth cone turning. *Bioessays.* 27:86–90.
5. Mitchison, T., and M. Kirschner. 1984. Dynamic instability of microtubule growth. *Nature.* 312:237–242.
6. Hill, T. L. 1984. Introductory analysis of the GTP-cap phase-change kinetics at the end of a microtubule. *Proc. Natl. Acad. Sci. USA.* 81:6728–6732.
7. Tanaka, E., and J. Sabry. 1995. Making the connection: cytoskeletal rearrangements during growth cone guidance. *Cell.* 83:171–176.
8. Tanaka, E., T. Ho, and M. W. Kirschner. 1995. The role of microtubule dynamics in growth cone motility and axonal growth. *J. Cell Biol.* 128:139–155.
9. Challacombe, J. F., D. M. Snow, and P. C. Letourneau. 1997. Dynamic microtubule ends are required for growth cone turning to avoid an inhibitory guidance cue. *J. Neurosci.* 17:3085–3095.
10. Suter, D. M., A. W. Schaefer, and P. Forscher. 2004. Microtubule dynamics are necessary for SRC family kinase-dependent growth cone steering. *Curr. Biol.* 14:1194–1199.
11. Verde, F., M. Dogterom, …, S. Leibler. 1992. Control of microtubule dynamics and length by cyclin A- and cyclin B-dependent kinases in *Xenopus* egg extracts. *J. Cell Biol.* 118:1097–1108.
12. Poulain, F. E., and A. Sobel. 2007. The "SCG10-LIke Protein" SCLIP is a novel regulator of axonal branching in hippocampal neurons, unlike SCG10. *Mol. Cell. Neurosci.* 34:137–146.
13. Riederer, B. M., V. Pellier, …, G. Grenningloh. 1997. Regulation of microtubule dynamics by the neuronal growth-associated protein SCG10. *Proc. Natl. Acad. Sci. USA.* 94:741–745.
14. Grenningloh, G., S. Soehrman, …, H. Cadas. 2004. Role of the microtubule destabilizing proteins SCG10 and stathmin in neuronal growth. *J. Neurobiol.* 58:60–69.
15. Morii, H., Y. Shiraishi-Yamaguchi, and N. Mori. 2006. SCG10, a microtubule destabilizing factor, stimulates the neurite outgrowth by modulating microtubule dynamics in rat hippocampal primary cultured neurons. *J. Neurobiol.* 66:1101–1114.
16. Morii, H., T. Yamada, …, N. Mori. 2006. Site-specific phosphorylation of SCG10 in neuronal plasticity: role of Ser^{73} phosphorylation by *n*-methyl D-aspartic acid receptor activation in rat hippocampus. *Neurosci. Lett.* 396:241–246.
17. Schaefer, A. W., N. Kabir, and P. Forscher. 2002. Filopodia and actin arcs guide the assembly and transport of two populations of microtubules with unique dynamic parameters in neuronal growth cones. *J. Cell Biol.* 158:139–152.
18. Geraldo, S., and P. R. Gordon-Weeks. 2009. Cytoskeletal dynamics in growth-cone steering. *J. Cell Sci.* 122:3595–3604.
19. Myers, K. A., I. Tint, …, P. W. Baas. 2006. Antagonistic forces generated by cytoplasmic dynein and myosin-II during growth cone turning and axonal retraction. *Traffic.* 7:1333–1351.
20. van Veen, M. P., and J. van Pelt. 1994. Dynamic mechanisms of neuronal outgrowth. *Prog. Brain Res.* 102:95–108.
21. van Veen, M. P., and J. van Pelt. 1994. Neuritic growth rate described by modeling microtubule dynamics. *Bull. Math. Biol.* 56:249–273.
22. Hely, T. A., and D. J. Willshaw. 1998. Short-term interactions between microtubules and actin filaments underlie long-term behavior in neuronal growth cones. *Proc. Biol. Sci.* 265:1801–1807.
23. Craig, E. M., D. van Goor, …, A. Mogilner. 2012. Membrane tension, myosin force, and actin turnover maintain actin treadmill in the nerve growth cone. *Biophys. J.* 102:1503–1513.
24. Kaláb, P., A. Pralle, …, K. Weis. 2006. Analysis of a RanGTP-regulated gradient in mitotic somatic cells. *Nature.* 440:697–701.
25. Niethammer, P., P. Bastiaens, and E. Karsenti. 2004. Stathmin-tubulin interaction gradients in motile and mitotic cells. *Science.* 303:1862–1866.
26. Wollman, R., E. N. Cytrynbaum, …, A. Mogilner. 2005. Efficient chromosome capture requires a bias in the 'search-and-capture' process during mitotic-spindle assembly. *Curr. Biol.* 15:828–832.
27. Athale, C. A., A. Dinarina, …, E. Karsenti. 2008. Regulation of microtubule dynamics by reaction cascades around chromosomes. *Science.* 322:1243–1247.
28. Aoki, K., T. Nakamura, …, M. Matsuda. 2007. An essential role for the SHIP2-dependent negative feedback loop in neuritogenesis of nerve growth factor-stimulated PC12 cells. *J. Cell Biol.* 177:817–827.
29. Neves, S. R., P. Tsokas, …, R. Iyengar. 2008. Cell shape and negative links in regulatory motifs together control spatial information flow in signaling networks. *Cell.* 133:666–680.
30. Burnette, D. T., A. W. Schaefer, …, P. Forscher. 2007. Filopodial actin bundles are not necessary for microtubule advance into the peripheral domain of *Aplysia* neuronal growth cones. *Nat. Cell Biol.* 9:1360–1369.

31. Schneider, C. A., W. S. Rasband, and K. W. Eliceiri. 2012. NIH Image to ImageJ: 25 years of image analysis. *Nat. Methods.* 9:671–675.
32. Burnette, D. T., L. Ji, …, P. Forscher. 2008. Myosin II activity facilitates microtubule bundling in the neuronal growth cone neck. *Dev. Cell.* 15:163–169.
33. Gittes, F., B. Mickey, …, J. Howard. 1993. Flexural rigidity of microtubules and actin filaments measured from thermal fluctuations in shape. *J. Cell Biol.* 120:923–934.
34. Mickey, B., and J. Howard. 1995. Rigidity of microtubules is increased by stabilizing agents. *J. Cell Biol.* 130:909–917.
35. Holy, T. E., M. Dogterom, …, S. Leibler. 1997. Assembly and positioning of microtubule asters in microfabricated chambers. *Proc. Natl. Acad. Sci. USA.* 94:6228–6231.
36. Laan, L., N. Pavin, …, M. Dogterom. 2012. Cortical dynein controls microtubule dynamics to generate pulling forces that position microtubule asters. *Cell.* 148:502–514.
37. Nadar, V. C., A. Ketschek, …, P. W. Baas. 2008. Kinesin-5 is essential for growth-cone turning. *Curr. Biol.* 18:1972–1977.
38. Klumpp, S., and R. Lipowsky. 2005. Cooperative cargo transport by several molecular motors. *Proc. Natl. Acad. Sci. USA.* 102: 17284–17289.
39. Kramers, H. 1940. Brownian motion in a field of force and the diffusion model of chemical reactions. *Physica.* 7:284–304.
40. Levchenko, A., J. Bruck, and P. W. Sternberg. 2000. Scaffold proteins may biphasically affect the levels of mitogen-activated protein kinase signaling and reduce its threshold properties. *Proc. Natl. Acad. Sci. USA.* 97:5818–5823.
41. Manna, T., D. A. Thrower, …, L. Wilson. 2009. Regulation of microtubule dynamic instability in vitro by differentially phosphorylated stathmin. *J. Biol. Chem.* 284:15640–15649.
42. Arnal, I., E. Karsenti, and A. A. Hyman. 2000. Structural transitions at microtubule ends correlate with their dynamic properties in *Xenopus* egg extracts. *J. Cell Biol.* 149:767–774.
43. Nedelec, F., and D. Foethke. 2007. Collective Langevin dynamics of flexible cytoskeletal fibers. *New J. Phys.* 9:427.
44. Kincaid, D. R., and E. W. Cheney. 2008. Numerical Mathematics and Computing. Thomson Learning, Florence, KY.
45. Crank, J. 1976. The Mathematics of Diffusion, 2nd Ed. Clarendon Press, Oxford, England.
46. Eaton, J. W. 2002. GNU Octave Manual. Network Theory Limited, UK. http://www.network-theory.co.uk/.
47. Kabir, N., A. W. Schaefer, …, P. Forscher. 2001. Protein kinase C activation promotes microtubule advance in neuronal growth cones by increasing average microtubule growth lifetimes. *J. Cell Biol.* 152:1033–1044.
48. Driver, J. W., D. K. Jamison, …, M. R. Diehl. 2011. Productive cooperation among processive motors depends inversely on their mechanochemical efficiency. *Biophys. J.* 101:386–395.
49. Dent, E. W., and F. B. Gertler. 2003. Cytoskeletal dynamics and transport in growth cone motility and axon guidance. *Neuron.* 40:209–227.
50. Dent, E. W., S. L. Gupton, and F. B. Gertler. 2011. The growth cone cytoskeleton in axon outgrowth and guidance. *Cold Spring Harb. Perspect. Biol.* 3. http://cshperspectives.cshlp.org/content/3/3/a001800.
51. Wang, P. Y., R. S. Petralia, …, S. D. Brenowitz. 2011. Functional NMDA receptors at axonal growth cones of young hippocampal neurons. *J. Neurosci.* 31:9289–9297.
52. Guirland, C., S. Suzuki, …, J. Q. Zheng. 2004. Lipid rafts mediate chemotropic guidance of nerve growth cones. *Neuron.* 42:51–62.
53. Brown, G. C., and B. N. Kholodenko. 1999. Spatial gradients of cellular phospho-proteins. *FEBS Lett.* 457:452–454.
54. Kholodenko, B. N., G. C. Brown, and J. B. Hoek. 2000. Diffusion control of protein phosphorylation in signal transduction pathways. *Biochem. J.* 350:901–907.
55. Baas, P. W., and O. I. Mozgova. 2012. A novel role for retrograde transport of microtubules in the axon. *Cytoskeleton* (*Hoboken*). 69:416–425.
56. Baas, P. W., and W. Yu. 1996. A composite model for establishing the microtubule arrays of the neuron. *Mol. Neurobiol.* 12:145–161.
57. Buck, K. B., and J. Q. Zheng. 2002. Growth cone turning induced by direct local modification of microtubule dynamics. *J. Neurosci.* 22:9358–9367.
58. Ming, G.-L., H.-J. Song, …, M. M. Poo. 1997. cAMP-dependent growth cone guidance by netrin-1. *Neuron.* 19:1225–1235.
59. Bouzigues, C., M. Morel, …, M. Dahan. 2007. Asymmetric redistribution of GABA receptors during GABA gradient sensing by nerve growth cones analyzed by single quantum dot imaging. *Proc. Natl. Acad. Sci. USA.* 104:11251–11256.
60. Pujic, Z., D. Mortimer, …, G. J. Goodhill. 2009. Assays for eukaryotic cell chemotaxis. *Comb. Chem. High Throughput Screen.* 12:580–588.
61. Moore, S. W., N. Biais, and M. P. Sheetz. 2009. Traction on immobilized netrin-1 is sufficient to reorient axons. *Science.* 325:166.
62. Mortimer, D., J. Feldner, …, G. J. Goodhill. 2009. Bayesian model predicts the response of axons to molecular gradients. *Proc. Natl. Acad. Sci. USA.* 106:10296–10301.
63. Bouzigues, C., D. Holcman, and M. Dahan. 2010. A mechanism for the polarity formation of chemoreceptors at the growth cone membrane for gradient amplification during directional sensing. *PLoS ONE.* 5:e9243.
64. Joanne Wang, C., X. Li, …, A. Levchenko. 2008. A microfluidics-based turning assay reveals complex growth cone responses to integrated gradients of substrate-bound ECM molecules and diffusible guidance cues. *Lab Chip.* 8:227–237.
65. Rosoff, W. J., J. S. Urbach, …, G. J. Goodhill. 2004. A new chemotaxis assay shows the extreme sensitivity of axons to molecular gradients. *Nat. Neurosci.* 7:678–682.
66. Hellal, F., A. Hurtado, …, F. Bradke. 2011. Microtubule stabilization reduces scarring and causes axon regeneration after spinal cord injury. *Science.* 331:928–931.
67. Medeiros, N. A., D. T. Burnette, and P. Forscher. 2006. Myosin II functions in actin-bundle turnover in neuronal growth cones. *Nat. Cell Biol.* 8:215–226.
68. Coppin, C. M., D. W. Pierce, …, R. D. Vale. 1997. The load dependence of kinesin's mechanical cycle. *Proc. Natl. Acad. Sci. USA.* 94:8539–8544.
69. Howard, J. 2001. Mechanics of Motor Proteins and the Cytoskeleton. Sinauer Associates, Sunderland, MA.